scientific reports

Check for updates

OPEN

High sensitivity tapered fiber refractive index biosensor using hollow gold nanoparticles

Parisa Borjikhani[1], Nosrat Granpayeh[1] & Mohammad Ismail Zibaii[2]✉

A localized surface plasmon resonance (LSPR) sensor based on tapered optical fiber (TOF) using hollow gold nanoparticles (HAuNPs) for measuring the refractive index (RI) is presented. This optical fiber sensor is a good candidate for a label-free RI biosensor. In practical biosensors, bioreceptors are immobilized on nanoparticles (NPs) that only absorb specific biomolecules. The binding of these biomolecules to the receptors changes the local RI around the sensor and this change is detected by the transmittance spectrum of the fiber. Fast, accurate, easy and low-cost disease diagnosis are the advantages of optical fiber biosensors. In this paper, the structure theory is reviewed and the sensor is simulated by the finite difference time domain (FDTD) method and the finite element method (FEM) and the effect of the thickness and diameter of the HAuNPs and the waist diameter of the TOF is investigated. For the structure with HAuNPs thickness (2.5 nm), diameter (50 nm), and the fiber waist diameter of 10 µm, the wavelength sensitivity of 489.8 nm/RIU and full width at half maximum (FWHM) of 50 nm are obtained, which are better than those specifications in some other LSPR fiber sensors. In addition, the sensitivity of the sensor increases about 2–3 times compared to those of sensors with the same structure. Although there are many parameters in human blood that can change its RI, in practical work, the special bioreceptors on the sensor can deactivate other markers except the specific cancer markers, which changes the effective RI. Therefore, this optical fiber sensor is used for label-free detecting the RI of cancer cells and can be used as a biosensor for the detection of early stages of cancers in a non-invasive way, just using human blood samples.

Keywords Localized surface plasmon resonance, Hollow gold nanoparticle, Tapered optical fiber, Refractive index biosensor, Cancer cell detection

At the beginning of the formation and growth of the primary cancer tumor, some cancer cells are released from the primary tumor and enter the bloodstream. Liquid biopsy, which means taking a blood sample and analyzing it, can lead to the detection of cancer cells in the blood and the diagnosis of cancer[1,2]. Diagnosing cancer in the early stages allows patients to use the best available treatment options to deal with it[3]. Some sensors can detect the presence of cancer biomolecules in human blood. Localized surface plasmon resonance (LSPR) optical fiber sensors have high sensitivity to detect blood refractive index (RI) variations and can be useful in disease diagnosis.

Noble metal nanoparticles (NPs) have unique optical and electrical properties[4]. LSPR is one of their optical properties in which incident light leads to collective oscillation of free electrons in NPs[5,6]. Hollow metal nanostructures are promising structures with a cavity showing unique plasmonic properties. Therefore, in applications such as sensing, Raman spectroscopy and drug delivery, hollow nanostructures are more useful than solid ones[7]. Nanospheres, nano stars, nano prisms, nano rings, nano rods, and nano cages are some forms of hollow nanostructures[8]. In hollow gold nanoparticles (HAuNPs), the interaction of plasmonic mode and cavity mode leads to a stronger resonance. In addition, they have good anti-corrosion properties and biocompatibility, which is useful for biomedical applications[8]. There are different methods for the synthesis and fabrication of nanostructures. One method includes three steps of preparing silica nanostructures as a template, forming a thick metal shell around the template, and then selectively removing the silica particles with HF solution[9].

The main advantages of optical fiber sensors are easy application, lightweight, low cost, immunity to electromagnetic interference and resistance to harsh environments[10]. The structure of an optical fiber sensor must be designed and modified in such a way that the light or evanescent field of the guided light penetrates the

[1]Center of Excellence in Electromagnetics, Optical Communication Laboratory, Faculty of Electrical Engineering, K.N. Toosi University of Technology, Tehran, Iran. [2]Laser and Plasma Research Institute, Shahid Beheshti University, Tehran, Iran. ✉email: m_zibaye@sbu.ac.ir

sensing medium around the fiber. For this purpose, polishing, chemical corrosion or heat-and-stretch methods for fabrication can be used[11,12]. U-shaped fiber[13], D-shaped fiber[14], tapered fiber[15], fiber Bragg grating[16], and long-period fiber grating[17] are some useful optical fiber structures. In the optical fiber biosensor, bioreceptors are immobilized on the fiber, and the binding of the target analyte as a sensing medium to the bioreceptor changes the effective RI, and these changes can be detected by the biosensor[18,19]. Biosensors can be used to detect markers of a disease in body fluids such as blood, urine, saliva, and sweat[20]. Many types of optical fiber sensors based on LSPR have been proposed to detect different analytes. Various materials such as graphene oxide[21] or zinc oxide[22] with gold NPs (AuNPs) have been used to provide LSPR based on tapered optical fiber (TOF) sensor. On the other hand, the TOF is one of the simplest optical fiber sensors[12]. Different structures of the TOF sensors such as simple tapered fiber[23], taper-in-taper structure[24], J-shaped fiber[25], S-shaped fiber[26], etc. have been proposed for biosensing applications. In addition, some LSPR sensors have been proposed to detect some factors such as alanine aminotransferase (ALT), which is a critical component of human blood and is associated with liver injury[24], uric acid[21], ascorbic acid[22], cholesterol level[27], and glucose level[28]. In diagnosing cancer in the early stages, imaging methods such as X-ray, magnetic resonance imaging (MRI), computed tomography (CT), endoscopy and ultrasound cannot be very effective[29]. Therefore, in several reports, NPs themselves have been used for early diagnosis and treatment of cancers[29–31]. It has been reported that some drugs using NPs can achieve better performance for destroying tumors[30]. With the help of HAuNPs, it is possible to have a promising technique for simultaneous trans-arterial tumor-targeted chemotherapy delivery and thermal ablation[32]. Some LSPR biosensors have high sensitivity for cancer detection[33]. Plasmonic tilted fiber Bragg grating and V-shaped plasmonic photonic crystal fiber biosensors have been presented to detect some types of cancers[34,35]. Colorectal, liver, prostate, ovarian, breast, lung, blood, cervical, oral, gastric/pancreatic, bladder, and skin cancers are some of the cancers that were diagnosed with them by sampling blood or other body fluids such as saliva and urine[29–35].

Previous reports show that the fabricated hollow NPs individually have better plasmonic properties and performance than those of solid NPs. The hybridization of the plasmons in hollow NPs results in the enhancement of the plasmon fields along with more homogeneous distribution as well as the reduction of LSPR quenching due to absorption. In addition, they have a higher detection limit and sensitivity and greater resonance in label-free sensing applications and due to their good anti-corrosiveness and biocompatibility, they are useful in biosensing applications[7,8]. However, to the best of our knowledge, the sensor structure using hollow NPs on the TOF has not been reported so far. In this paper, a TOF sensor based on the LSPR method using HAuNPs is investigated in different aspects to increase the RI sensitivity for label-free cancer sensing using cancer biomarkers from blood samples in liquid biopsy. The advantages of this method over other methods such as open surgical biopsy and needle biopsy are non-invasiveness, less risk and pain, real-time detection, and easier reproducibility[1,2]. The advantages of the optical fiber biosensing method over other methods is its label-free detection, rapid response, biocompatibility, high sensitivity, and its portability[36,37].

Key features of this design are enhancing the amplitude and penetration depth of evanescent field in the fiber sensor based on biconical tapering and LSPR effect which leads to an increase in the RI sensitivity of the sensor in the tapered region. The TOF RI sensors show excellent sensitivity with a fast response time in the local change of RI, which has enormous potential for real-time and label-free biosensing. In addition, the immobilization of the NPs on the TOF significantly increases RI sensitivity by creating the LSPR property that engages the electrons in the NPs to oscillate in coupling with the evanescent wave. Additionally, AuNPs are stable and resistant to oxidation, making them more durable for long-term applications. Also, in integrating of the TOF with HAuNPs, interaction of the plasmonic mode and the cavity mode in HAuNPs creates a stronger resonance and significantly increases the wavelength sensitivity compared to solid AuNPs[8].

The remaining of the paper is organized as follows; in Sect. 2, the structure and its characteristics, the theory and the simulation method are introduced. The effect of different dimensions of the sensor and the possibility of detection of the analyte RI, especially the RI of the cancer cells are examined in Sect. 3. Finally, the paper is concluded in Sect. 4.

Materials and analysis method

Sensor characteristics

As shown in Fig. 1, the sensor probe is an optical fiber with a cladding diameter of 125 µm and a core diameter of 8 µm, which is tapered at the waist. The waist diameter of d_w is in the range of 10–18 µm. The NPs are HAuNPs with a diameter of d_{out} in the range of 40–60 nm and a shell thickness of t in the range of 2.5–17.5 nm which are immobilized on the waist of the TOF. The analyte around the sensor has the RI of n_a in the range of 1.333–1.403. The TOF waist area is pure silica[15] and its RI is calculated by the Sellmeier formula[38]. The RIs of the HAuNP are derived from the Johnson and Christy experimental data[39]. The surface density of AuNPs in experimental TOF sensors can be in the range of 1.77×10^{11} m^{-2} – 3.7×10^{14} m^{-2}[40,41]. The surface density of HAuNPs in this work is 3.185×10^{12} m^{-2}. Therefore, the number of HAuNPs considered in our simulations is 100,000. This number is obtained from the average approximation of the number of AuNPs used on experimental TOF sensors to match modeling and experimental specifications[40,41].

The reason for using the TOF for sensing is that compared to conventional optical fibers, TOF can create a larger local electric field and as a result, a higher evanescent field and large penetration depth in the tapered area due to the smaller radius of the waist. Therefore, tapering is another way of modifying the optical fiber for improving the sensitivity of fiber sensor to measuring RI by enhancing the effect of evanescent field in cladding part. The TOF is a good candidate for label free sensing based on RI sensing in biosensing applications. On the other hand, the sensing effect of TOF can be improved due to the large surface area at the tapered structure, which can better contact the analyte. In addition, TOF is compact and can be flexibly installed for measurement in various environments due to ease of integration and better compatibility. The TOF does not require complicated process and expensive materials, and its preparation is easier[42,43].

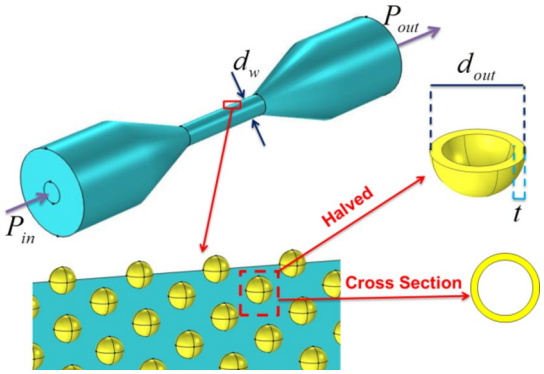

Fig. 1. Schematic of the TOF sensor with HAuNPs on its waist.

Theory and simulation method

When the V-number of the small core fiber is less than unity, most of the core light power is guided in the cladding[15]. It is feasible to assume negligible excess loss for adiabatic TOF, therefore, in this case, only fundamental mode (LP_{01}) is considered to transmit in the TOF waist[44]. So, the theoretical model of the TOF can be assumed as a cylindrical waveguide (fiber waist) whose surrounding is infinite[44].

In general, the simulation of AuNPs on the waist of the TOF must be done in the three-dimensional space, because the structure is not uniform in the longitudinal direction. In addition, due to the large number of NPs and the large difference between the dimensions of the NP and the fiber, it is difficult to simulate its complete structure in three-dimensional space to get the field coupling between the plasmonic and core modes. Therefore, we use a combination of equations and simulations to obtain the sensor response of the TOF with HAuNPs on the waist. The transmitted power of TOF with HAuNPs on the waist region can be derived as[40,45]:

$$P_{out} = P_{in} \exp\left(-\pi d_w \frac{NC_{ext}}{A_{eff}} L\right) \tag{1}$$

where P_{in}, P_{out} ,d_w, and L are input power, output power, the diameter and the length of the waist, respectively. N is the number of HAuNPs per unit area, while the total number of HAuNPs is $m = \pi d_w LN$. In addition, C_{ext} is the extinction cross-section of the HAuNP that is the energy extinction rate to incident irradiance ratio[46], and A_{eff} is the effective mode area on the surface of the waist which is related to the Poynting vector distribution, S_z, of the fundamental mode[40,45]:

$$A_{eff} = \frac{\int_{A\to\infty} \mathrm{S_z} \cdot \mathrm{dA}}{S_z|_{d=d_w}} \tag{2}$$

In Eq. (2), the numerator is the surface integral of the Poynting vector distributed on the entire surface, including the cross-sectional area perpendicular to the axis of the TOF waist and its surroundings, and the denominator is the magnitude of the Poynting vector distributed on the TOF waist with the diameter of d_w.

The TOF waist is simulated separately by the FEM to calculate the effective mode area, A_{eff}, and the HAuNP is simulated separately by the finite difference time domain (FDTD) method to calculate the extinction cross-section, C_{ext}. Then using Eq. (1), the transmittance spectrum of the TOF with HAuNPs around its waist is calculated as a TOF-LSPR sensor. The cross-section of the TOF waist without HAuNPs is shown in Fig. 2a, which is surrounded by analyte and the perfectly matched layer (PML) boundary conditions. The denominator of Eq. (2) is the distribution of the Poynting on the TOF waist, as shown by the blue line in Fig. 2a. Figure 2b shows the electric field distribution of the fundamental mode in the TOF waist.

Figure 2a The cross-section of the TOF waist which is surrounded by analyte and the PML boundary conditions and (b) the electric field norm (electric field amplitude) of the fundamental mode in the TOF waist.

To calculate C_{ext}, Mie theory is used and the NP is simulated in three-dimensional space by the FDTD method, because this method is suitable in terms of memory and CPU usage to simulate the NP. The thickness of the HAuNP must be less than skin depth of the metal, until the electric field can penetrate the cavity. The RI of metal can be assumed as $n = \sqrt{\epsilon_r + i\epsilon_i}$, where ϵ_r and ϵ_i are the real and imaginary parts of the dielectric function, respectively, which the imaginary part depends on the conductivity of the metal. Therefore, the skin depth equation is proved as follows[47,48]:

$$\delta = \frac{\lambda_0}{2\pi\,\mathrm{Im}(n)} \tag{3}$$

where λ_0 is the free space wavelength and $\mathrm{Im}(n)$ is the imaginary part of the RI of the metal. In experimental studeis, HAuNPs typically have a shell thickness of 2.5–22.5 nm[7]. Skin depth spectrum of Au for wavelengths less than 2 μm shows that these thicknesses are almost less than skin depth. Therefore, in this wavelength range, the

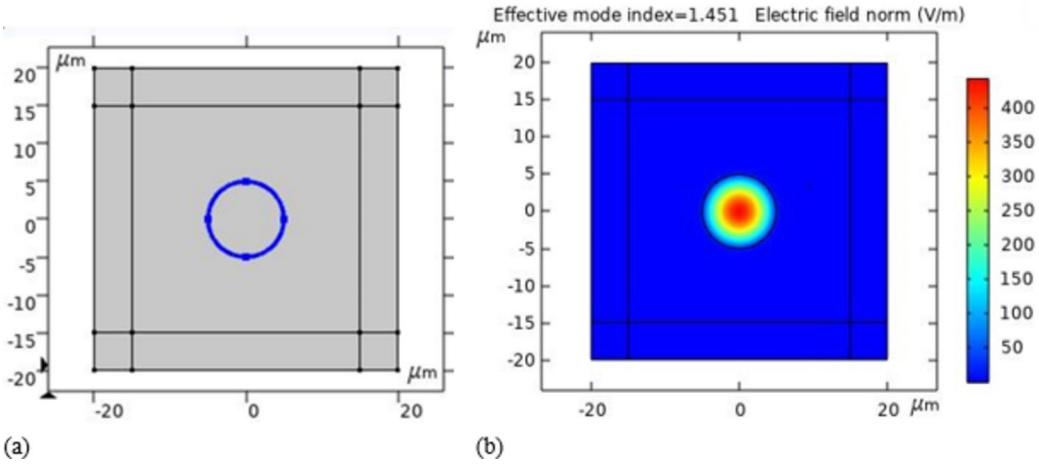

Fig. 2. (**a**) The cross-section of the TOF waist which is surrounded by analyte and the PML boundary conditions and (**b**) the electric field norm (electric field amplitude) of the fundamental mode in the TOF waist

electric field penetrates into the cavity of the HAuNPs[47]. Figure 3 shows the electric field in HAuNPs with shell thicknesses of 20 nm and 2.5 nm. These two values with low and high thicknesses have been selected from the range of thicknesses that are usually used to make HAuNPs[7].

In Fig. 3b,c, it can be seen that by increasing the shell thickness from 2.5 nm to 20 nm, the electric field penetrating the HAuNP weakens about ten times. Plasmons induce surface charges on the inner and outer surfaces of the metal shell. Due to the low thickness of the shell, metal and cavity plasmons interact with each other, and in fact, this interaction is controlled by the thickness of the metal shell. The interaction of plasmons of the inner and outer surfaces of the shell creates two hybridized plasmonic modes, one of which is related to the asymmetric coupling of modes with high energy and the other one is related to the symmetric coupling of modes with low energy[49]. Plasmonic hybridization leads to an increase in the plasmonic field and its more homogeneous distribution, and for a thinner NP, a stronger coupling between the charges of the inner and outer surfaces leads to a red shift and an improvement of the near field[49]. The absorption and scattering cross-section spectra for HAuNPs are shown in Fig. 3 (d) which the LSPR peak is at 863 nm. Unlike the solid NP, which for diameters less than 60 nm, the scattering cross-section is negligible and the extinction cross-section is almost equal to the absorption cross-Sect[46], in Fig. 3e, it can be seen that the scattering cross-section is significant for the HAuNP and to calculate the extinction cross-section, it is necessary to add the scattering and absorption cross- sections together. Figure 3e shows that the absorption cross-section of the HAuNP is 4.5 times higher than that of the solid NP.

Results and discussion

Effect of different aspects on sensing

The sensor transmittance spectra for different thicknesses of the HAuNP are shown in Fig. 4a. With decreasing the HAuNP thickness from 17.5 to 2.5 nm, the amplitude of the transmittance dip decreases from approximately 0.86 to 0.37 and the wavelength of the dip increases by 300 nm. In Fig. 4b, the purple curve shows the wavelength sensitivity and the orange curve shows the full width at half maximum (FWHM) of the structure. Obtained results show that decreasing the shell thickness causes the resonance dip of the transmittance spectrum to become deeper, because reducing the shell thickness increases the penetration of the electric field.

Figure 4b shows that as the shell thickness decreases, the sensitivity increases, but on the other hand, the FWHM also increases slightly. For example, in Fig. 4b, it can be seen that by reducing the shell thickness from 7.5 nm to 2.5 nm, the sensitivity and FWHM increase up to 1.7 and 1.3 times, respectively.

Figure 5a shows the transmittance spectra of the structure with variation of the outer diameter of HAuNPs. It can be seen that with the increase of the outer diameter of the HAuNPs, the dip of the transmittance spectrum becomes deeper, so that, with increasing the outer diameter from 40 to 60 nm, the amplitude of the transmittance dip decreases from approximately 0.53 to 0.37 and the wavelength of the dip increases by 128.6 nm. The reason is that the increase in the outer diameter of the HAuNP causes the cavity to become larger and the surface area of the gold shell to increase, both of which lead to an increase in the resonance of the transmittance spectrum. By increasing the HAuNP outer diameter, the sensitivity and FWHM increase gradually. As shown in Fig. 5a, the changes in the sensor transmittance spectrum are uniform and due to this uniform response, the sensor transmittance spectrum can be predicted up to the HAuNP outer diameter of 80 nm. Here, the transmittance spectrum response stops at the HAuNP outer diameter of 60 nm. Because with larger outer diameters, the FWHM increases, which is not desirable[23].

Figure 5b shows the transmittance spectra of the sensor with variation in the TOF waist diameter. It is shown that as the TOF waist diameter decreases, the dip of the transmittance spectrum becomes deeper. Because, as the TOF waist diameter decreases, the leakage evanescent field from the TOF waist to the outer medium increases. Therefore, the transmission is reduced and the dip becomes deeper. For example, by reducing the TOF waist diameter from 18 μm to 10 μm, the transmission dip reduced about two times. In general, in TOFs with a smaller

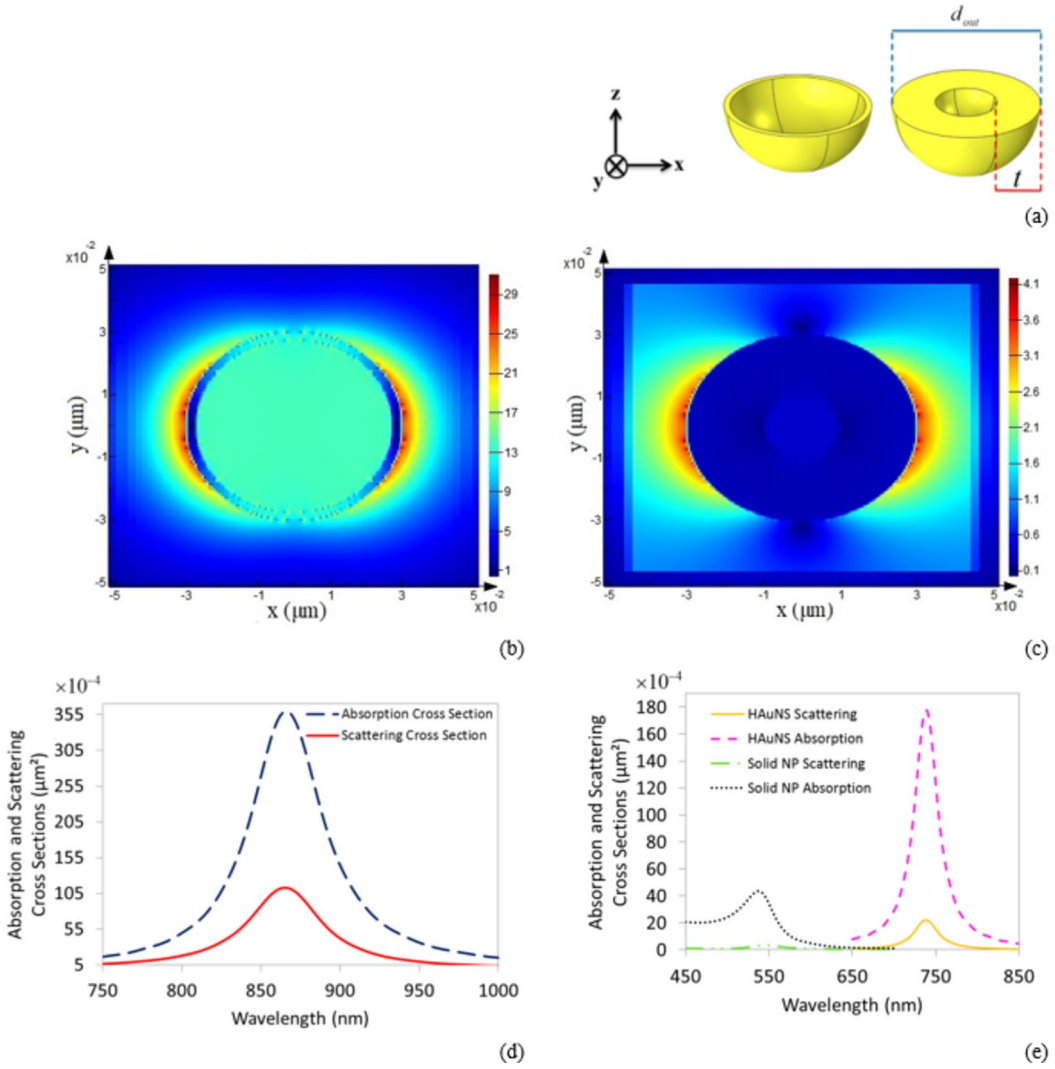

Fig. 3. (**a**) Two HAuNPs with different shell thicknesses of t, (**b**) electric field distribution in HAuNP with shell thickness of 2.5 nm and (**c**) 20 nm at a wavelength of 863 nm, (**d**) absorption and scattering cross-section spectra for the HAuNP for t=2.5 nm, d_{out} =60 nm, and (**e**) absorption and scattering cross-section spectra for the solid NP with diameter of 40 nm and HAuNP with t=2.5 nm, d_{out} =40 nm, the incidence of light in z direction (its electric field in x-direction).

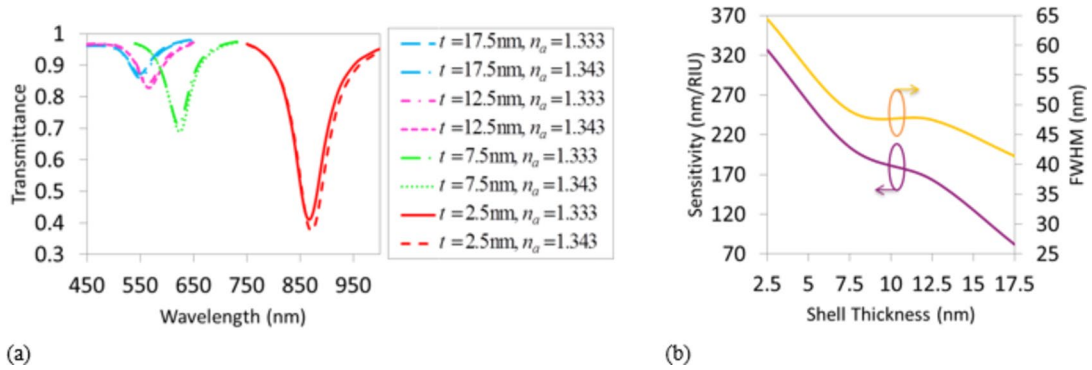

Fig. 4. (**a**) The transmittance spectra of the TOF sensor with HAuNPs on its waist in two analyte RIs of 1.333 and 1.343, (**b**) the wavelength sensitivity and FWHM of the sensor vs. the variation of the HAuNP thickness for d_{out} = 60 nm, and $_{dw}$ = 10 μm

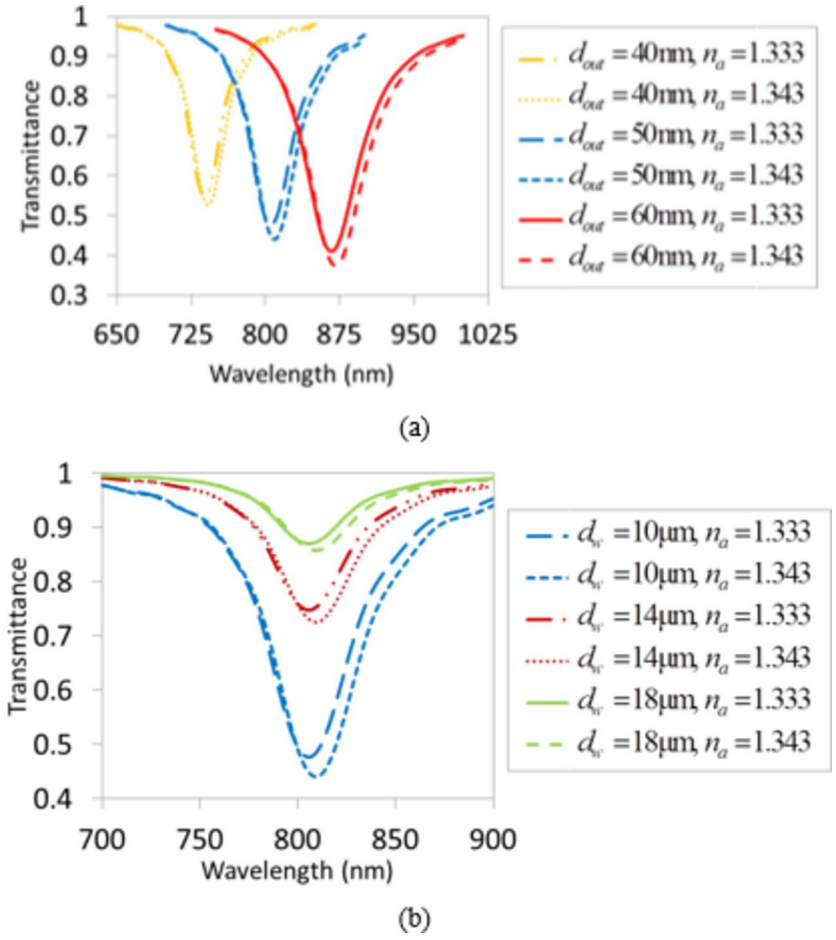

Fig. 5. The transmittance spectra of the TOF sensor with HAuNPs on its waist (**a**) vs. the variation of the outer diameter of the HAuNPs for t=2.5 nm and dw = 10 μm, (**b**) vs. the variation of the TOF waist diameter for t=2.5 nm and d_{out} = 50 nm in two analyte RIs of 1.333 and 1.343

waist diameter, the interaction of the fiber evanescent field with the surrounding medium is higher, which leads to stronger resonance for the HAuNPs on the TOF waist. But on the other hand, it is better to consider the sensor's robustness for practical works, as well. TOF waist diameters less than 10 μm are not desirable in this work because they will significantly reduce the sensor's robustness[50].

Refractive index sensing

Figure 6 shows the transmittance spectra of the sensor versus the variation of analyte RI. It can be seen that the variation of analyte RI is well detected with the wavelength dip shift. The RI sensitivity and the FWHM of the structure with t = 2.5 nm, d_{out}=50 nm, and d_w=10 μm were obtained 489.8 nm/RIU and 50 nm, respectively. These sizes were selected according to the dimensions of HAuNP and TOF in experimental papers. According to obtained results from Figs. 4 and 5, the designed structure has more sensitivity and less FWHM. The RI of the analyte around the waist region of the fiber is assumed to be in the range of 1.333–1.403, which is related to biological materials for biomolecular sensing applications[41]. According to Fig. 6, because of the distinction of the transmittance spectra in each RI, this structure can be used for label-free biosensor based on RI sensing.

Detection of cancer cells

In the TOF-LSPR sensor fabrication, a chemical method can be used to immobilize HAuNPs to the TOF surface as schematically shown in Fig. 7. For this purpose, first, the optical fiber is treated with piranha solution to form hydroxyl groups. Then, the TOF was immersed in 5% aminopropyldimethylethoxysilane (APMES) diluted in isopropanol for 90 min. Self-assembled monolayer (SAM) prepared by APMES contains Si head groups and amine functional groups to form silanol bonds with hydroxyl groups on the optical fiber surface. This means that the substrate will be positively charged by amine functionalization, which is used to immobilize the negatively charged AuNPs. Finally, the optical fiber is immersed in a colloidal AuNPs solution that has been prepared by citrate reduction. The gold surface is negatively charged by citrate and electrostatically bound to the amine groups[51].

In biosensing applications, for various analytes and diseases such as triacylglycerides, SARS-CoV-2, etc[52–54]. , specific receptors can be immobilized on NPs and according to Fig. 8, the binding of some analyte biomarkers

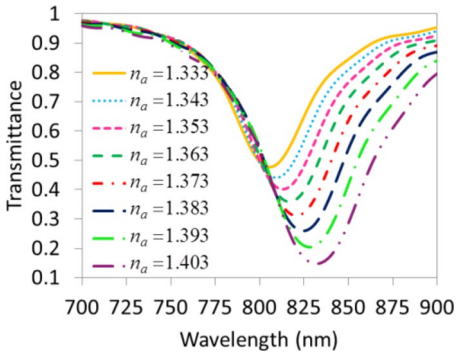

Fig. 6. The transmittance spectra of the TOF sensor with HAuNPs on its waist vs. the variation of analyte RI for $t = 2.5$ nm, $d_{out} = 50$ nm, and $d_w = 10$ µm.

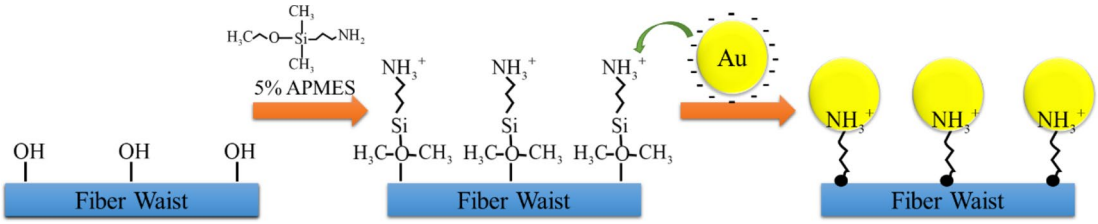

Fig. 7. Schematic of chemical bonding in practical application of LSPR fiber sensor.

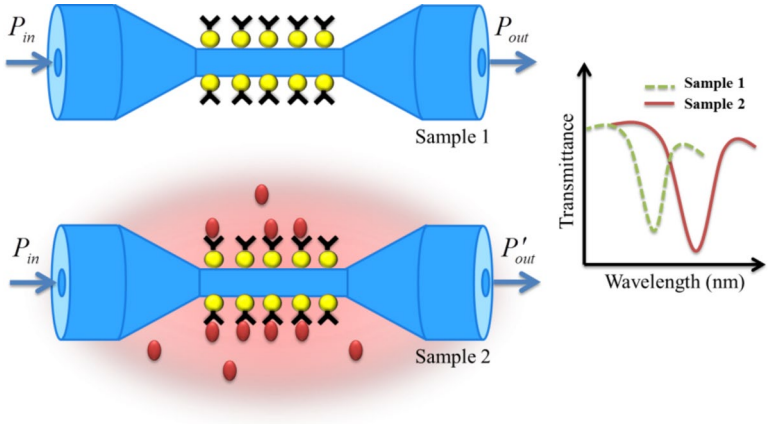

Fig. 8. Schematic design of two TOF-LSPR sensors with receptors on the NPs and their transmittance spectra, sample 1 without analyte and sample 2 with analyte and binding of biomarkers to receptors in sample 2.

around the sensor to these receptors changes the effective RI or concentration, and these variations can be detected through the transmittance spectrum of the TOF-LSPR sensor.

As shown in the TOF-LSPR sensor scheme in Fig. 8, the bioreceptors are immobilized on NPs. In experiments, for selectivity of the biosensors, some bioreceptors such as antibodies, enzymes, aptamers or DNA can be used.

Although there are many parameters in human blood that can change its RI, the special bioreceptors on the sensor that are for the specific cancer markers can deactivate other markers and hence the measured variation of blood RI is due to the cancerous effects[55–57]. Cancer cells have a higher RI than normal cells, because they have more protein[58]. Therefore, the presence of cancer cells in human blood can be detected by changing the RI of blood. Table 1 shows the size, RI and cell liquid concentration of skin, cervical, blood, adrenal gland, and breast cancers compared to the normal state[58–68].

When the blood is in contact with the biosensor, the difference in its RI can be recognized according to Fig. 9, in which the dip of the transmittance spectrum of the sensor at each RI is at a different wavelength. Therefore, each cancer can be diagnosed by its specific transmittance spectrum

It should be noted that in practice, by binding disease specific biological receptors on HAuNPs, only the biomolecules of that disease bind to the receptors and change the effective RI[40]. Other biomolecules, even if they

Cell name	Cell size	Cell type	Concentration level	Refractive index
Basal	30 µm	Normal cell	30-70%	1.360
		Skin cancer	80%	1.380
Hela	17.66 µm	Normal cell	30-70%	1.368
		Cervical cancer	80%	1.392
Jurkat	13-20 µm	Normal cell	30-70%	1.376
		Blood cancer	80%	1.390
PC-12	30-40 µm	Normal cell	30-70%	1.381
		Adrenal gland cancer	80%	1.395
MDA-MB-231	18.72 µm	Normal cell	30-70%	1.385
		Breast cancer I	80%	1.399
MCF-7	20 µm	Normal cell	30-70%	1.387
		Breast cancer II	80%	1.401

Table 1. The size, RI and cell liquid concentration of some cancers compared to the normal state [58–68]

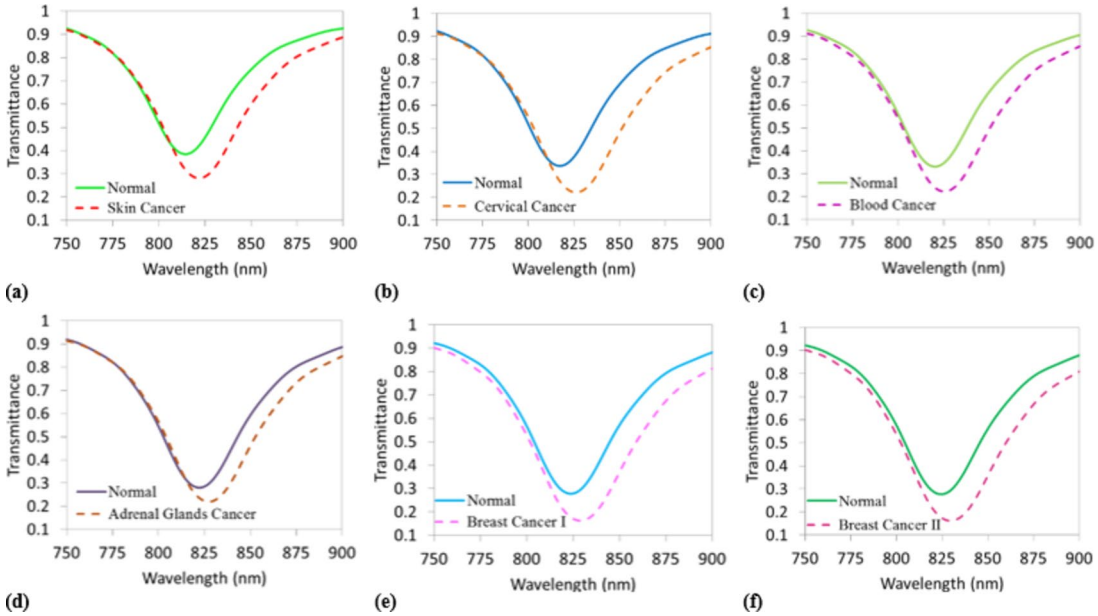

Fig. 9. The transmittance spectra of the TOF sensor with HAuNPs on its waist surrounded by blood with the RI of some cancers and the normal state for t=2.5 nm, d_{out} =50 nm, and dw=10µm

have the same RI as the investigated diseases, will not bind to the receptors and will not change the effective RI. Therefore, this structure is an RI sensor that can be useful in practical biosensors.

The comparison of the proposed TOF-LSPR sensor with some reported optical fiber sensors is provided in Table 2. According to Table 2, the FWHM in our structure is 20% of that of the structure with Au-reinforced Ag nanoprisms[45]. In addition, it can be seen that our structure has the highest wavelength sensitivity among these compared sensors. The wavelength sensitivity of the TOF-LSPR sensor in this work is about 1.3 to 4 times higher than that of LSPR fiber tip sensors, slightly higher than that of LSPR fiber with removed cladding, 1.7 to 4 times more than that of multi-tapered fiber sensors, 1.27 times more than that of TOF with Au-reinforced Ag nano prisms, 2 times more than that of S-shaped tapered fiber sensor, and 1.3 times more than that of tapered fiber with long-period grating sensor.

The wavelength sensitivity and RI range of each sensor based on the sensor number according to the results of Table 2 are shown in Fig. 10. In addition to high sensitivity, it can be seen that in this work (No. 13) the range of the analyte RI in which the sensor behaves linearly is a relatively wide range compared to other structurs which can be useful for sensing a wide range of analytes.

Therefore, a key feature of using AuNPs instead of silver NPs is the stability and resistance to oxidation of the AuNPs, which makes them more durable for long-term applications[80]. On the other hand, the results show that the wavelength sensitivity for the TOF sensor with solid AuNPs is very low[23]. While using the HAuNPs for sensing according to the Table 2 not only increases the wavelength sensitivity, but also significantly reduces the FWHM.

No.	Optical fiber sensor type	Nanomaterial	Analyte refractive Index	FWHM (nm)	Sensitivity (nm/RIU)	Reference
1	Optical fiber tip	Au nanodot arrays	1-1.377	-	196	[69]
2	Optical fiber with removed cladding	AuNPs	1.36–1.43	-	471	[70]
3	Optical fiber tip	AuNPs	1-1.378	-	195.72	[71]
4	Optical fiber tip	Au Nanostructure Pattern	1.333–1.378	-	125	[72]
5	Multi-tapered optical fiber	-	1.33–1.38	-	226.6	[73]
6	Optical fiber tip	AuNPs	1.33–1.37	-	387	[74]
7	Multi-tapered optical fiber	-	1.333–1.3737	-	261.9	[75]
8	Double-tapered optical fiber	-	1.333–1.359	-	126.15	[76]
9	Double-tapered photonic crystal fiber	-	1.333–1.3737	-	281.6	[77]
10	Tapered optical fiber	Au-Reinforced Ag Nanoprisms	1.333–1.383	250	385	[45]
11	Tapered fiber with long-period gratings	-	1.333–1.456	-	372	[78]
12	S-Shaped tapered fiber	-	1.332–1.387	-	268.8	[79]
13	Tapered optical fiber	HAuNPs	1.333–1.403	50	489.8	This Work

Table 2. Comparison of some optical fiber sensors.

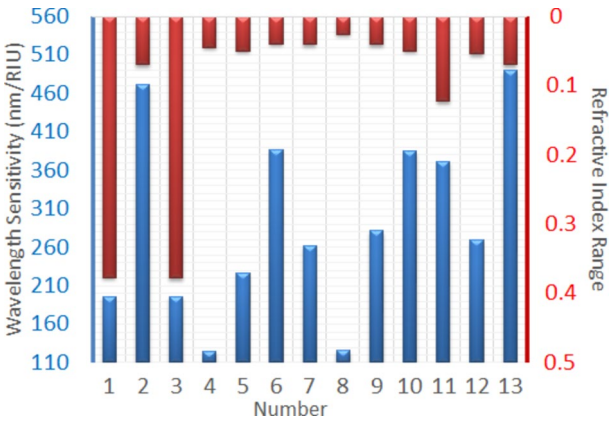

Fig. 10. The wavelength sensitivity and RI range of each sensor based on the sensor number given in Table 2.

Furthermore, obtained results in Fig. 3e indicated that the resonance amplitude of the solid AuNPs in comparison with the HAuNPs is very low, and to compensate for this, a much larger number of solid AuNPs must be immobilized on the sensor.

Experimental challenges

However, it is important to study some experimental challenges that may cause the response to deviate from the simulation result. Some fabrication parameters such as the diameter and length of the TOF and the diameter and number of NPs can affect to experimental results. The results show that for a TOF with a taper diameter of 10 µm and a taper length of 1 mm, a deviation of 2 µm in diameter and 0.25 mm in length is acceptable, and this range of variation does not significantly affect the sensing result[23]. However, it is recommended to use more precise fabrication based on heat pulling methods. In general, the TOF with a taper diameter of at least 3 µm and a taper length of 0.95 to 7.5 mm can be fabricated[15]. The sensitivity of the RI sensor increases with increasing taper length and decreasing taper diameter. However, if these changes are large, the robustness of the sensor decreases[50]. Therefore, a trade-off between sensitivity and robustness is required, so the designed structure in this work with a taper diameter of 10 µm and a taper length of 1 mm would have the appropriate characteristics of sensitivity and robustness.

In addition, to produce high-quality TOFs, it should be considered some properties such as high adiabaticity, uniform waist diameter, and low surface roughness[81]. The surface roughness of the fiber is an effective factor in the sensor response[82]. However, the results show that the silica TOFs can be fabricated with very smooth surfaces (with surface roughness less than 1 nm) and minimizing the surface roughness reduces the surface scattering[83].

Changes in the number of NPs also cause small changes in the response that can be neglected[23,84]. However, variations in the size of the HAuNPs will have a more effect on the response. Therefore, it is important to prepare them in a precise manner so that the average diameter of the fabricated NPs is equal to that in the simulation[36]. The citrate reduction route is a suitable method for the synthesis of AuNPs. The formation of NPs can be confirmed by ultraviolet–visible and high-resolution transmission electron microscopy (HRTEM) data[85]. The absorption spectra of AuNPs at different days after synthesis show that the absorption wavelength peak remains unchanged, indicating its stability[84]. The coverage of AuNPs on the TOF surface will influence the sensitivity of

the LSPR-TOF sensor. In experimental studies some attempts have been made to achieve uniform deposition of AuNPs[86,87], but completely uniform deposition of AuNPs on the fiber is not easily possible. Therefore, in this simulation, the distribution of AuNPs was not uniform and the distance between Au NPs was not important. According to Eq. (1), only the extinction cross-section of the NP and the total number of NPs affect the output power. However, the aggregation of NPs can change the wavelength sensitivity. The results show that the aggregation of NPs increases the wavelength sensitivity by at least 50 nm/RIU[23].

The calibration process, ambient temperature variation, and sensitivity to movement are some other experimental challenges[88]. Packaging the sensor in a glass tube using UV adhesive helps to minimize environmental impacts[84]. In this method, special chambers are provided on the glass tube to hold the sensor and allow the analyte to enter and contact the sensor and exit[84]. The results show that pressure changes up to 0.1 MPa do not have much effect on the sensor response[89]. However, in label free fiber biosensors based on RI sensing, temperature variation may affect the sensor response. Typically in blood samples, it should be considered that the temperature does not change by more than 10 °C[90,91]. Therefore, the effect of temperature on the LSPR-TOF RI sensor must be considered. In general, the LSPR-TOF sensors show excellent repeatability and reversibility[36,85].

Conclusion

A tapered optical fiber (TOF) with hollow gold nanoparticles (HAuNPs) on its waist region as the localized surface plasmon resonance (LSPR) sensor was simulated using finite difference time domain (FDTD) method and the finite element method (FEM). The range of the HAuNP thickness values was determined according to the skin depth. In addition, the variations of the thickness, the diameter of the HAuNPs, and the waist diameter of the TOF on the transmission spectrum were demonstrated. For the structure with HAuNPs thickness and diameter of 2.5 nm and 50 nm respectively and the fiber waist diameter of 10 μm, the ability of the structure for refractive index (RI) sensing was examined. The wavelength sensitivity and full width at half maximum (FWHM) of the proposed TOF-LSPR sensor using HAuNPs in the analyte RI range of 1.333 to 1.403 were obtained 489.8 nm per refractive index unit (nm/RIU) and 50 nm, respectively. The results were compared to some similar sensors, and it was observed that in this work the sensitivity was about two to four times that of the several sensors of multi-tapered fiber, LSPR fiber tip, and S-shaped tapered fiber. On the other hand, the obtained results showed the ability of the sensor to detect the RIs of skin, cervical, blood, adrenal gland and breast cancer cells with cell liquid concentration of 80%. Therefore, this structure can be useful in practical biosensors for label-free and early detection of different types of cancer based on specific receptors.

Data availability

Data underlying the results presented in this paper are not publicly available at this time but may be obtained from the corresponding author upon reasonable request.

Received: 1 September 2024; Accepted: 6 January 2025
Published online: 09 January 2025

References

1. Qi, Z. H. et al. The significance of liquid biopsy in pancreatic cancer. *J. Cancer*. **9**, 3417–3426 (2018).
2. Alix-Panabières, C. & Pantel, K. Clinical applications of circulating tumor cells and circulating tumor dna as liquid biopsy. *Cancer Discov*. **6**, 479–491 (2016).
3. Zahra, Q., ul ain, Khan, Q. A. & Luo, Z. Advances in optical aptasensors for early detection and diagnosis of various cancer types. *Front. Oncol.* **11**, 632165(1–7) (2021).
4. Li, M. X. et al. Distance mediated electrochemiluminescence enhancement of CdS thin films induced by the plasmon coupling of gold nanoparticle dimers. *Chem. Commun.* **52**, 14230–14233 (2016).
5. Zhao, J., Zhang, X., Yonzon, C. R., Haes, A. J. & Van-Duyne, R. P. Localized surface plasmon resonance biosensors. *Nanomed* **1**, 219–228 (2006).
6. Dombi, P. et al. Strong-field nano-optics. *Rev. Mod. Phys.* **92**, 025003(1–66) (2020).
7. Genç, A. et al. Hollow metal nanostructures for enhanced plasmonics: synthesis, local plasmonic properties and applications. *Nanophotonics* **6**, 193–213 (2017).
8. Park, J. M., Choi, H. E., Kudaibergen, D., Kim, J. H. & Kim, K. S. Recent advances in hollow gold nanostructures for biomedical applications. *Front. Chem.* **9**, 6992841–6992817 (2021).
9. Abdollahi, S. N., Naderi, M. & Amoabediny, G. Synthesis and characterization of hollow gold nanoparticles using silica spheres as templates. *Colloids Surf. Physicochem Eng. Asp*. **436**, 1069–1075 (2013).
10. Gupta, B. D., Shrivastav, A. M. & Usha, S. P. Surface plasmon resonance-based fiber optic sensors utilizing molecular imprinting. *Sensors* **16**, 1381(1–33) (2016).
11. Iadicicco, A. et al. Evanescent wave sensor based on permanently bent single mode optical fiber. *Sens. Actuators B Chem.* **155**, 903–908 (2011).
12. Korposh, S., James, S. W., Lee, S. W. & Tatam, R. P. Tapered optical fibre sensors: current trends and future perspectives. *Sensors* **19**, 2294(1–39) (2019).
13. Tan, A. J. Y., Ng, S. M., Stoddart, P. R. & Chua, H. S. Trends and applications of U-shaped fiber optic sensors: a review. *IEEE Sens. J.* **21**, 120–131 (2021).
14. Cennamo, N. et al. D-shaped plastic optical fibre aptasensor for fast thrombin detection in nanomolar range. *Sci. Rep.* **9**, 1–9 (2019).
15. Leung, A., Rijal, K., Shankar, P. M. & Mutharasan, R. Effects of geometry on transmission and sensing potential of tapered fiber sensors. *Biosens. Bioelectron.* **21**, 2202–2209 (2006).
16. Guo, T., Liu, F., Guan, B. O. & Albert, J. Tilted fiber grating mechanical and biochemical sensors. *Opt. Laser Technol.* **78**, 19–33 (2016).
17. Janczuk-Richter, M. et al. Long-period fiber grating sensor for detection of viruses. *Sens. Actuators B Chem.* **250**, 32–38 (2017).
18. Campaña, A. L. et al. Enzyme-based electrochemical biosensors for microfluidic platforms to detect pharmaceutical residues in wastewater. *Biosensors* **9** (41), 1–21 (2019).
19. Monk, D. J. & Walt, D. R. Optical fiber-based biosensors. *Analyt Bioanalyt chem.* **379**, 931–945 (2004).
20. Bhalla, N., Jolly, P., Formisano, N. & Estrela, P. Introduction to biosensors. *Essays Biochem.* **60**, 1–8 (2016).

21. Singh, L. et al. LSPR based uric acid sensor using graphene oxide and gold nanoparticles functionalized tapered fiber. *Opt. Fiber Technol.* **53**, 102043(1–8) (2019).
22. Zhu, G. et al. Tapered optical fiber-based LSPR biosensor for ascorbic acid detection. *Photonic Sens.* **11**, 418–434 (2021).
23. Borjikhani, P., Zibaii, M. I. & Granpayeh, N. Sensitivity enhancement of the LSPR-based tapered optical fiber biosensor by variation of nanoparticle arrangement. *JOSA B*. **40**, 2968–2978 (2023).
24. Wang, Z. et al. Taper-in-taper fiber structure-based LSPR sensor for alanine aminotransferase detection. *Opt. Express*. **29**, 43793–43810 (2021).
25. Ning, W. et al. An ultrasensitive J-shaped optical fiber LSPR aptasensor for the detection of Helicobacter pylori. *Anal. Chim. Acta*. **1278**, 341733 (2023).
26. Li, G., Singh, R., Guo, J., Zhang, B. & Kumar, S. Nb2CTx MXene-assisted double S-tapered fiber-based LSPR sensor with improved features for tyramine detection. *Appl. Phys. Lett.* **122**, 083701(1–5) (2023).
27. Kumar, S. et al. LSPR-based cholesterol biosensor using a tapered optical fiber structure. *Biomed. Opt. Express*. **10**, 2150–2160 (2019).
28. Li, G. et al. Graphene oxide/multiwalled carbon nanotubes assisted serial quadruple tapered structure-based lspr sensor for glucose detection. *IEEE Sens. J.* **22**, 16904–16911 (2022).
29. Zhang, Y., Li, M., Gao, X., Chen, Y. & Liu, T. Nanotechnology in cancer diagnosis: progress, challenges and opportunities. *J. Hematol. Oncol. J. Hematol. Oncol.* **12**, 137(1–13) (2019).
30. Alrushaid, N., Khan, F. A., Al-Suhaimi, E. A. & Elaissari, A. Nanotechnology in cancer diagnosis and treatment. *Pharmaceutics* **15**, 1025(1–22) (2023).
31. Perfézou, M., Turner, A. & Merkoçi, A. Cancer detection using nanoparticle-based sensors. *Chem. Soc. Rev.* **41**, 2606–2622 (2012).
32. Sheth, R. A. et al. Doxorubicin-loaded hollow gold nanospheres for dual photothermal ablation and chemoembolization therapy. *Cancer Nanotechnol.* **11** (6), 1–16 (2020).
33. Tai, J., Fan, S., Ding, S. & Ren, L. Gold nanoparticles based optical biosensors for cancer biomarker proteins: a review of the current practices. *Front. Bioeng. Biotechnol.* **10**, 8771931–8771916 (2022).
34. Chen, X. et al. Label-free detection of breast cancer cells using a functionalized tilted fiber grating. *Biomed. Opt. Express*. **13**, 2117–2129 (2022).
35. Abdelghaffar, M. et al. Highly sensitive V-shaped SPR PCF biosensor for cancer detection. *Opt. Quantum Electron.* **55**, 472(1–20) (2023).
36. Singh, L. et al. Gold nanoparticles and uricase functionalized tapered fiber sensor for uric acid detection. *IEEE Sens. J.* **20**, 219–226 (2020).
37. Arefnia, F. et al. Citrate polymer optical fiber for measuring refractive index based on LSPR sensor. *Sci. Rep.* **14**, 18637(1–19) (2024).
38. Ghatak, A. & Thyagarajan, K. *An Introduction to fiber Optics* (Cambridge University Press, 1998).
39. Johnson, P. B. & Christy, R. W. Optical constants of the noble metals. *Phys. Rev. B*. **6**, 4370–4379 (1972).
40. Li, K., Zhou, W. & Zeng, S. Optical micro/nanofiber-based localized surface plasmon resonance biosensors: fiber diameter dependence. *Sensors* **18**, 3295(1–11) (2018).
41. Lin, H. Y., Huang, C. H., Cheng, G. L., Chen, N. K. & Chui, H. C. Tapered optical fiber sensor based on localized surface plasmon resonance. *Opt. Express*. **20**, 21693–21701 (2012).
42. Zhang, W. et al. Advances in tapered optical fiber sensor structures: from conventional to novel and emerging. *Biosensors* **13** (644), 1–37 (2023).
43. Ban, S. & Lian, Y. The structure and applications of fused tapered fiber optic sensing: a review. *Photonics* **11**, 414(1–28) (2024).
44. Zhu, S. et al. High sensitivity refractometer based on TiO2-coated adiabatic tapered optical fiber via ALD technology. *Sensors* **16**, 1295(1–11) (2016).
45. Wieduwilt, T. et al. Gold-reinforced silver nanoprisms on optical fiber tapers—A new base for high precision sensing. *APL Photonics* **1**, 066102(1–11) (2016).
46. Li, K. et al. Gold nanoparticle amplified optical microfiber evanescent wave absorption biosensor for cancer biomarker detection in serum. *Talanta* **120**, 419–424 (2014).
47. Sallam, M. O., Vandenbosch, G. A. E., Gielen, G. & Soliman, E. A. Integral equations formulation of plasmonic transmission lines. *Opt. Express*. **22**, 22388–22402 (2014).
48. Wooten, F. *Optical Properties of Solids* (Academic, 1972).
49. Wiley, B. J. et al. Maneuvering the surface plasmon resonance of silver nanostructures through shape-controlled synthesis. *J. Phys. Chem. B*. **110**, 15666–15675 (2006).
50. Shi, J., Xiao, S., Yi, L. & Bi, M. A sensitivity-enhanced refractive index sensor using a single-mode thin-core fiber incorporating an abrupt taper. *Sensors* **12**, 4697–4705 (2012).
51. Kim, H. M., Kim, H. J., Park, J. H. & Lee, S. K. High-performance biosensor using a sandwich assay via antibody-conjugated gold nanoparticles and fiber-optic localized surface plasmon resonance. *Anal. Chim. Acta* **1213**, 339960(1–8) (2022).
52. Baliyan, A., Usha, S. P., Gupta, B. D., Gupta, R. & Sharma, E. K. Localized surface plasmon resonance–based fiber-optic sensor for the detection of triacylglycerides using silver nanoparticles. *J. Biomed. Opt.* **22**, 107001(1–10) (2017).
53. Lu, M., Zhu, H., Bazuin, C. G., Peng, W. & Masson, J. F. Polymer-templated gold nanoparticles on optical fibers for enhanced-sensitivity localized surface plasmon resonance biosensors. *ACS Sens.* **4**, 613–622 (2019).
54. Luo, Z. et al. T-shaped aptamer-based lspr biosensor using Ω-shaped fiber optic for rapid detection of SARS-CoV-2. *Anal. Chem.* **95**, 1599–1607 (2023).
55. Eswaran, M. et al. & Mijakovic I. A Road map toward field-effect transistor biosensor technology for early stage cancer detection. *Small Methods* **6**, 2200809(1–20) (2022).
56. Wang, Y. et al. Targeted sub-attomole cancer biomarker detection based on phase singularity 2D nanomaterial-enhanced plasmonic biosensor. *Nano-Micro Lett.* **13**, 96(1–11) (2021).
57. Bellassai, N., D'Agata, R., Jungbluth, V. & Spoto, G. Surface plasmon resonance for biomarker detection: advances in non-invasive cancer diagnosis. *Front. Chem.* **7**, 473690(1–16) (2019).
58. Liang, X. J., Liu, A. Q., Lim, C. S., Ayi, T. C. & Yap, P. H. Determining refractive index of single living cell using an integrated microchip. *Sens. Actuators Phys.* **133**, 349–354 (2007).
59. Alimirzaie, S., Bagherzadeh, M. & Akbari, M. R. Liquid biopsy in breast cancer: a comprehensive review. *Clin. Genet.* **95**, 643–660 (2019).
60. Ayyanar, N., Raja, T. & Sharma, G. Sriram Kumar, D. Photonic crystal fiber-based refractive index sensor for early detection of cancer. *IEEE Sens. J.* **18**, 7093–7099 (2018).
61. Kharazmi, P., AlJasser, M. I., Lui, H., Wang, Z. J. & Lee, T. K. Automated detection and segmentation of vascular structures of skin lesions seen in dermoscopy, with an application to basal cell carcinoma classification. *IEEE J. Biomed. Health Inf.* **21**, 1675–1684 (2017).
62. Jafari, B. et al. Highly sensitive label-free biosensor: graphene/CaF2 multilayer for gas, cancer, virus, and diabetes detection with enhanced quality factor and figure of merit. *Sci. Rep.* **13**, 16184(1–15) (2023).
63. Baraty, F. & Hamedi, S. Label-free cancer cell biosensor based on photonic crystal ring resonator. *Results Phys.* **46**, 106317–106311 (2023).

64. Rahad, R., Rakib, A. K. M., Haque, M. A., Sharar, S. S. & Sagor, R. H. Plasmonic refractive index sensing in the early diagnosis of diabetes, anemia, and cancer: an exploration of biological biomarkers. *Results Phys.* **49**, 106478(1–13) (2023).
65. Yasli, A. Cancer detection with surface plasmon resonance-based photonic crystal fiber biosensor. *Plasmonics* **16**, 1605–1612 (2021).
66. Moon, H. S. et al. -Il. Continual collection and re-separation of circulating tumor cells from blood using multi-stage multi-orifice flow fractionation. *Biomicrofluidics* **7**, 014105(1–9) (2013).
67. Yang, T. et al. Determination of the membrane transport properties of jurkat cells with a microfluidic device. *Micromachines* **10**, 832(1–12) (2019).
68. Hu, R. et al. A novel method of neural differentiation of PC12 cells by using Opti-MEM as a basic induction medium. *Int. J. Mol. Med.* **41**, 195–201 (2018).
69. Lin, Y., Zou, Y., Mo, Y., Guo, J. & Lindquist, R. G. E-beam patterned gold nanodot arrays on optical fiber tips for localized surface plasmon resonance biochemical sensing. *Sensors* **10**, 9397–9406 (2010).
70. Lee, H., Kim, H. J., Park, J. H., Jeong, D. H. & Lee, S. K. Effects of surface density and size of gold nanoparticles in a fiber-optic localized surface plasmon resonance sensor and its application to peptide detection. *Meas. Sci. Technol.* **21**, 085805(1–9) (2010).
71. Lin, Y., Zou, Y. & Lindquist, R. G. A reflection-based localized surface plasmon resonance fiber-optic probe for biochemical sensing. *Biomed. Opt. Express*. **2**, 478–484 (2011).
72. Consales, M. et al. Lab-on-fiber technology: toward multifunctional optical nanoprobes. *ACS Nano*. **6**, 3163–3170 (2012).
73. Wang, P. et al. Enhanced refractometer based on periodically tapered small core singlemode fiber. *IEEE Sens. J.* **13**, 180–185 (2013).
74. Sciacca, B. & Monro, T. M. Dip biosensor based on localized surface plasmon resonance at the tip of an optical fiber. *Langmuir* **30**, 946–954 (2014).
75. Zhao, Y., Cai, L. & Hu, H. F. Fiber-optic refractive index sensor based on multi-tapered SMS fiber structure. *IEEE Sens. J.* **15**, 6348–6353 (2015).
76. Fu, S., Dai, H., Shi, Q. & Peng, B. A refractive index sensor based on the tapering theory. *IEEE Sens. J.* **16**, 954–957 (2016).
77. Zhao, Y., Xia, F. & Li, J. Sensitivity-enhanced photonic crystal fiber refractive index sensor with two waist-broadened tapers. *J. Light Technol.* **34**, 1373–1379 (2016).
78. Mullaney, K., Staines, S. E., James, S. W. & Tatam, R. P. Optimized process for fabricating ultrashort tapered long-period gratings. *J. Light Technol.* **36**, 1091–1096 (2018).
79. Chen, C. et al. Compact refractive index sensor based on an S-tapered fiber probe. *Opt. Mater. Express*. **8**, 919–925 (2018).
80. Dong, P., Lin, Y., Deng, J. & Di, J. Ultrathin gold-shell coated silver nanoparticles onto a glass platform for improvement of plasmonic sensors. *ACS Appl. Mater. Interfaces*. **5**, 2392–2399 (2013).
81. Harun, S. W., Lim, K. S., Tio, C. K., Dimyati, K. & Ahmad, H. Theoretical analysis and fabrication of tapered fiber. *Optik* **124**, 538–543 (2013).
82. Zhong, N. et al. Effects of surface roughness on optical properties and sensitivity of fiber-optic evanescent wave sensors. *Appl. Opt.* **52**, 3937–3945 (2013).
83. Healy, N., Sparks, J. R., Sazio, P. J. A., Badding, J. V. & Peacock, A. C. Tapered silicon optical fibers. *Opt. Express*. **18**, 7596–7601 (2010).
84. Kumari, A., Vyas, V. & Kumar, S. Synthesis, characterization, and applications of gold nanoparticles in development of plasmonic optical fiber-based sensors. *Nanotechnology* **34**, 042001(1–17) (2022).
85. Hidayat, N. et al. Sensitivity enhancement of gold nanospheres assisted CO2 laser tapered optical fiber for refractive index sensor. *Opt. Fiber Technol.* **77**, 103275(1–12) (2023).
86. Kim, H. M., Park, J. H. & Lee, S. K. Fiber optic sensor based on ZnO nanowires decorated by au nanoparticles for improved plasmonic biosensor. *Sci. Rep.* **9**, 15605(1–9) (2019).
87. Fakhri, M. A. et al. U. A gold nanoparticles coated unclad single mode fiber-optic sensor based on localized surface plasmon resonance. *Sci. Rep.* **13**, 5680(1–20) (2023).
88. Cano Perez, J. L. et al. & Rojas Laguna, R. Fiber optic sensors: a review for glucose measurement. *Biosensors* 11, 61(1–19) (2021).
89. Choi, S. et al. Tapered length dependence of pressure sensitivity in polarimetric fiber pressure sensor based on tapered high birefringence fiber. *IEEE Sens. J.* **20**, 2492–2503 (2020).
90. Jin, Y. L., Chen, J. Y., Xu, L. & Wang, P. N. Refractive index measurement for biomaterial samples by total internal reflection. *Phys. Med. Biol.* **51**, N371–379 (2006).
91. Sagor, R. H., Hassan, M. F., Sharmin, S., Adry, T. Z. & Emon Md.A.R. Numerical investigation of an optimized plasmonic on-chip refractive index sensor for temperature and blood group detection. *Results Phys.* **19**, 103611(1–11) (2020).

Author contributions

Parisa Borjikhani performed the simulations and drafted the manuscript. Nosrat Granpayeh and Mohammad Ismail Zibaii designed the structure and revised the manuscript.

Declarations

Competing interests

The authors declare no competing interests.

Additional information

Correspondence and requests for materials should be addressed to M.I.Z.